JOURNAL OF PROPULSION AND POWER
Vol. 21, No. 4, July–August 2005

Numerical Simulations in Scramjet Combustion with Boundary-Layer Bleeding

Toshinori Kouchi*
Tohoku University, Miyagi 980-8579, Japan
Tohru Mitani†
Japan Aerospace Exploration Agency, Miyagi 981-1525, Japan
and
Goro Masuya‡
Tohoku University, Miyagi 980-8579, Japan

Airframe-integrated scramjet engines swallow the boundary layers that develop on the forebody of space planes. The scramjet engine easily falls into engine stall (engine unstart) as a result of the boundary-layer separation resulting from combustion. In this study, to investigate the unstart characteristics, numerical simulations of a whole scramjet engine with boundary-layer bleeding are performed by using a reacting flow code, and the physics determining the engine performance is examined. Our computations well reproduce the engine combustion tests results with bleeding. Bleeding of 0.65% in a captured airflow suppresses the separation of the ingested boundary layer and extends the start limit from the fuel equivalence ratio of 0.5 to 1.0. The numerical results predict small discrete circular flames anchored around individual fuel jets near the injectors. These discrete flames merge to form a large envelope diffusion flame in the downstream portion of the combustor, as a result of the secondary flow produced by high pressure of the cowl shock and intensive combustion. This merged structure causes a large mass of unburned fuel and restricts the combustion efficiency and the thrust performance.

Nomenclature

D_{add}	=	additive drag in inlet
D_{int}	=	engine internal drag
H	=	engine height
Hc	=	captured height
M	=	Mach number
P	=	static pressure
Pw	=	wall pressure
q	=	dynamic pressure
qw	=	heat flux
T	=	static temperature
Tw	=	wall temperature
x	=	streamwise direction
Yi	=	mass fraction
y	=	height-wise direction
z	=	spanwise direction
ΔF	=	thrust increment with combustion
Δt	=	time step
η_c	=	air capture ratio
τw	=	wall share stress
Φ	=	bulk fuel equivalence ratio

Subscript

1	=	incoming flow

Presented as Paper 2003-7038 at the AIAA 12th International Space Planes and Hypersonic Systems and Technologies Conference, Norfolk, VA, 15–19 December 2003; received 31 January 2004; revision received 6 November 2004; accepted for publication 7 November 2004.

*Graduate Student, Department of Aeronautics and Space Engineering, 6-6-01 Aoba, Aramaki, Aoba, Sendai; kouchi@kakuda.jaxa.jp.

†Head, Space Propulsion Research Center, 1 Kimigaya, Koganesawa, Kakuda.

‡Professor, Department of Aeronautics and Space Engineering, 6-6-01 Aoba, Aramaki, Aoba, Sendai.

I. Introduction

AIRFRAME-INTEGRATED scramjet engines swallow the thick boundary layers that develop on the airframe of space planes. Scramjet engines must be therefore tested under conditions of boundary-layer ingestion in ground tests. The ingested boundary layer might be separated by the combustion-generated shock waves. The separation of the ingested boundary-layer promotes engine stall (termed "engine unstart" hereafter). To prevent the engine unstart and to extend the engine operating range, a boundary-layer bleeding system[1] was attached to the engine and tested under Mach 6 (M6) flight conditions at the RamJet Engine Test Facility (RJTF). Although the boundary-layer bleeding extended the operating range and doubled the net thrust,[2] the mechanism that suppresses engine unstart by the bleeding was not clarified because of difficulties in measurements of engine test.

Computational fluid dynamics (CFD) can provide valuable insight to complex hypersonic combustion flowfields.[3–6] If these computational results can be calibrated with experimental data, CFD can become a powerful tool that complements engine tests. Hosangadi et al.[3] employed the adaptive grid method to calculate flowfields in a scramjet combustor. They examined wall pressure distribution for verification of their computations. Goyne et al.[4,5] conducted numerical simulation of their combustor in cases of fuel-off, fuel-air mixing with and without reaction. They verified the CFD by both particle-image-velocimetry and fuel-plume-imaging results in addition to wall pressure.

Few simulations of whole scramjet engine with combustion, however, have been conducted. There has been no CFD validation with more important engine performance data such as drag/thrust, inlet performance, and thermal load. The purpose of this paper is to conduct numerical simulations of whole engine and to verify the CFD code by the engine performance data in addition to the wall pressure distributions. These calibrated computations are employed to understand the physics feature governing the engine performance in combustion tests with the bleeding.

The paper begins with a description of the experiment and its reliability. The numerical model employed is briefly described. Then the computational results are compared with the engine test data including wall pressure, heat flux, thrust/drag, and inlet performance

to validate the CFD code. The predictions of the verified computations identify the mechanism that suppresses the engine unstart resulting from boundary-layer bleeding and reveal the flame structure in the scramjet combustor which determines the combustion performance.

II. Experimental and Numerical Techniques

A. Flow Condition and Engine Configuration

1. Nozzle Flow

The experimental investigation was conducted at the RJTF. The facility nozzle supplies test gas simulating airflow at stagnation conditions of 4.8 MPa and a total temperature of 1500 K realized by a storage air heater. The test gas is expanded to Mach 5.3 through a two-dimensional, contoured nozzle. The static conditions at the nozzle exit are 250 K and 5.4 kPa. These conditions correspond to the scramjet engine inlet conditions for flight Mach number 6.

2. Engine Geometry

Our scramjet engine is illustrated in Fig. 1. This engine is rectangular with a length of 2.1 m, and its entrance and exit are 200 mm in width and 250 mm in height H. It consists of a cowl, a topwall, and two sidewalls. It is divided into four sections: an inlet, an isolator, a combustor, and a nozzle section.

In Fig. 1, the airstream flows from the left to the right and is compressed in the sidewall compression-type inlet. This inlet consists of 6-deg wedges. Its leading edge is swept back by 45 deg to spill the airflow from the inlet and to improve the inlet starting performance. A strut can be installed to this engine, as shown by the shaded area in Fig. 1. In the present study, the engine was tested with a 30-mm-thick strut, by which the geometrical contraction ratio was 5.00.

This engine has rearward-facing steps with a height of 4 mm on the sidewalls and of 2 mm on the topwall at the entrance of the combustor. There are 12 fuel injectors downstream of the steps on each sidewall. The injectors are located at 16 mm downstream from the steps in the combustor. Hydrogen fuel at room temperature is injected perpendicular to the airflow at sonic speed from each orifices with a diameter of 1.5 mm. The orifices are equally spaced, and the distance between the adjacent orifices are 20 mm in y direction. The stoichiometric fuel mass flow rate is 145 g/s because the air capture ratio η_c evaluated from our computations is 0.83. Details on these inlet performances will be presented later. A spark-initiated, H2/O2 torch-igniter is installed on the topwall of the engine because the M6 flight conditions is located on a boundary of autoignition limit. Details of the torch igniter are shown in Ref. 7.

The forebody boundary layer is simulated by the boundary layer developed on the facility nozzle. Figure 1 presents the boundary-layer bleed device[1] installed on the topwall. It consists of a perforated plate, a water-cooled heat exchanger, a choked orifice, and an ON/OFF valve. The perforated plate is attached between the exit of the inlet and the middle of the isolator. The bleeding flow rate was measured using the orifice and was found to be 30 g/s. This bleeding rate was fixed during the tests. Details on the boundary-layer bleed device can be found in Ref. 1.

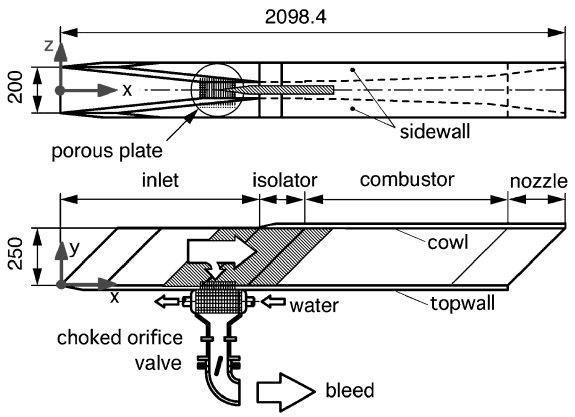

Fig. 1 Scramjet engine installing boundary-layer bleed system. The x, y, and z axes are stream, height, and spanwise, respectively.

B. Measurement Reliability

In our engine tests, wall pressure, wall temperature, heat flux, and forces acting on engines were measured. The wall pressure was monitored at about 170 taps on the walls inside the engine. Experimental uncertainty of the wall pressure was within $\pm 2\%$. Wall temperature was measured at about 30 points by thermocouples embedded in the engine walls. The heat flux was measured by two independent methods: measurement with a heat-flux meter and calculation using the wall temperature histories. The heat flux obtained by the thermocouples was compared with that measured by the heat-flux meter, and the reliability of the heat-flux measurement was verified.[8] Heat-flux data had uncertainty of $\pm 15\%$, which was estimated by changing wall temperature during the engine test.

Thrust, lift, and pitching moment were monitored by a force measurement system, consisting of load cells. The engine drag was measured in the fuel-off condition. The drag decreased as a result of combustion with the H_2-fuel injection. This drag reduction is termed thrust increment ΔF. In addition, the ΔF can be independently calculated from the difference between the integration of the wall pressure in the combustion case and that of the fuel-off case.[9,10] The reliability in thrust measurement is estimated by comparing these two-thrust increments.[9]

C. Numerical Methods

1. Algorithm

The numerical method employed consisted of the full three-dimensional compressible Reynolds-averaged Navier–Stokes equations with finite-rate chemistry. The solution algorithm[6] was based on a cell-vertex, upwind, finite volume scheme for an arbitrarily shaped cell. Spatial integration was performed with the advection upstream splitting method with flux-difference-splitting and flux-vector-splitting scheme.[11] The second-order spatial accuracy was realized by a linear reconstruction of the primitive gas dynamic variables with Venkatakrishnan's limiter.[12] The computational efficiency was greatly improved by the lower-upper symmetric Gauss-Seidel[13] implicit method with a reordering algorithm for an unstructured hybrid grid. In this code, the thermodynamic properties of gases were calculated by using the JANAF tables.[14] The algorithm adopted the finite-rate hydrogen-oxygen reaction,[15] which consisted of nine species (H_2, O_2, H_2O, H, HO_2, OH, O, H_2O_2, and N_2)/17 elementary reactions.

The turbulent eddy viscosity was evaluated by the one-equation turbulence model proposed by Goldberg and Ramakrishnan.[16] This turbulence model does not require a procedure for searching along lines normal to the walls, which is required in the Baldwin–Lomax algebraic model. Thus, it is suitable for an unstructured hybrid grid. The turbulent Prandtl number was 0.9, and the turbulent Schmidt number was 1.0. The dependence of computations on the turbulent model was investigated for several nonreacting configurations related to scramjet engine computations.[17]

The computations were performed on a NEC SX-6 cluster using up to 64 processors (8 GFLOPS/CPU). The parallelization was based on message-passing interface. An 8- or 40-grid sequence was used for convergence acceleration. The CPU time required for a turbulent flow simulation without reactions was approximately 12 h with the maximum time step Δt of 10^{-5} s (Courant–Friedrichs–Lewy number $= 10^5$). The maximum residual of the discretized equations was reduced by six orders of magnitude after approximately 6000 iterations. After activating chemical reactions, a steady-state solution required about $600 \sim 1200$ hours, and the residual reached its minimum value after falling for three orders of magnitude (maximum $\Delta t = 10^{-8}$).

2. Boundary Condition

To simulate the M6 combustion tests in the RJTF, the inflow conditions of the engine inlet were set so that the Mach number M_1, static pressure P_1 and static temperature T_1 were 5.3, 5.4 kPa, and

250 K, respectively. The dynamic pressure q_1 of the incoming flow was 100 kPa. The Reynolds number based on the engine height was 2.1×10^6. The ingested boundary-layer thickness was 50 mm, based on the pitot pressure survey results[18] of the facility nozzle. The displacement and momentum thickness were 20.1 and 2.92 mm, respectively.

The injector was simulated by triangular cells on the surface of the combustor wall with imposed density, temperature, and velocity equal to the jet conditions. At the bleeding region shown in Fig. 1, flow speed normal to the wall was specified to impose the bleeding flow rate, and the other flow properties were determined by zeroth-order extrapolation. All solid walls were nonslip and isothermal, with a wall temperature Tw of 300 K. The effects of the wall temperature will be discussed later. For computations, the wall share stress and the heat flux were calculated by using the velocity and temperature gradient on the walls. These gradients were evaluated by a method based on 'Gauss' theorem.

3. Grid Optimization and Convergence

The three-dimensional computational region was composed of an unstructured hybrid grid[19] for accurate and efficient computations as well as ease of grid generation for a complex configuration. In this study, the simulation was performed on the internal domain of the engine over half of the spanwise width shown in Fig. 1 (assuming symmetry with the $z = 0$ plane). This domain consisted of approximately 1.3-million control volumes.

The hybrid grid was composed of tetrahedrons, prisms, and pyramids. The basic grid in our scramjet was a 7-mm tetrahedron. The size of tetrahedrons in the upstream region of the combustor was refined to 2.0 mm and that around the fuel injectors was 0.1 mm. The prismatic semistructured grid generated for viscous boundaries on the surfaces allowed control of the minimum spacing required for resolving viscous sublayers, thus ensuring the quality of the solution for high-Reynolds-number flows without diminishing the advantage of the flexibility of the unstructured grid. In the present study, the minimum distance from the wall was set to be 10^{-6} m. This minimum spacing of the prisms made the $y+$ on the walls lower than four even with combustion.

The grid convergence was checked by the calculations using the two grid modes: inlet model and combustor model calculations. In the inlet model, the streamwise grid density was doubled, and the minimum spacing near the walls was 10 times smaller than that of the whole engine model, and the effects of the streamwise grid on the Pw and the inlet performance were investigated. The streamwise Pw distribution in the inlet model showed good agreement with that of the engine model. In addition, the captured mass flow rate did not change.

In the combustor model, the effects of the grid density on the Pw, thrust, and combustion/mixing efficiencies were investigated. In addition, the effects of the minimum spacing near the walls on the transport properties and the flow separation as a result of combustion were checked. In Fig. 2, for example, the configuration of the combustor model with the coarse grid and the wall pressure distributions along the sidewall is shown for three different grid-refinement levels: coarse, medium, and fine. The coarse grid consisted of 10-mm tetrahedrons. The size of tetrahedrons near the fuel injector was refined to 4.0 mm. The medium grid consisted of 5- and 2.0-mm tetrahedrons. The fine grid consisted of 2- and 1.0-mm tetrahedrons. In this calculation with combustion, the inflow conditions were uniformly set on mass-weighted one-dimensional quantities evaluated from the inlet computations. Out of this analysis, it was found that the region near the fuel injector should be decided with cell smaller than 2 mm. These grid-convergence studies made the present scramjet grid optimized.

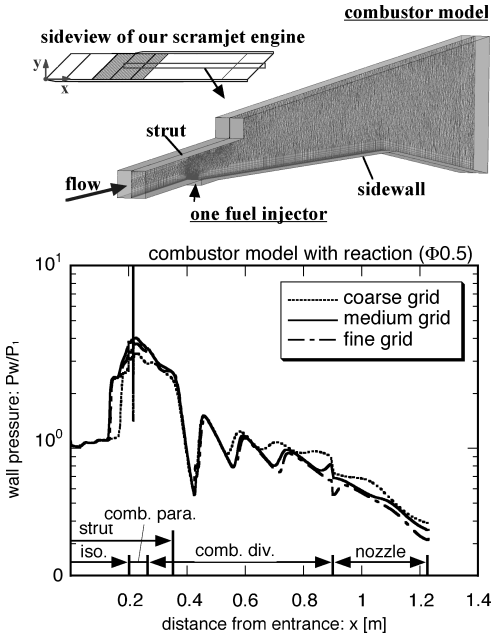

Fig. 2 Scramjet combustor model (coarse grid) and surface pressure distribution on sidewall for refined grids.

III. Validation of CFD

A. Wall Pressure and Heat-Flux Distribution

1. Wall Pressure Distribution

To validate the CFD code, the numerical results (lines) are compared with the experimental data (symbols). Figure 3 presents the Pw distributions on the sidewall at $y/H = 0.5$. The broken line and the triangular symbols denote the results for the fuel-off case, whereas the solid line and the circular symbols are those for the combustion case at the bulk equivalence ratio Φ of 1.0 with boundary-layer bleeding. Experimental uncertainty is comparable to the scale of the symbols in Fig. 3. The abscissa is the distance from the leading edge of the topwall normalized by the engine height H. The distances x/H of 2.97, 3.97, and 6.57 are those of the exits of the inlet, the isolator, and the combustor, respectively. The strut is attached between $x/H = 2.79$ and 4.37. The Pw is normalized by the upstream dynamic pressure q_1.

For the case of fuel-off shown by the broken line, the Pw in the inlet stepwise increases twice. The first rise between $x/H = 0.5$ and 2.6 is caused by the shock wave generated at the leading edge of the opposite sidewall. The second rise from 0.11 to 0.36 is caused by the impingement of the reflected sidewall shock wave at x/H of 2.6. The predicted Pw on the line of $y/H = 0.5$ can be compared with that obtained by the two-dimensional inviscid shock-wave analysis assuming a swept-back wedge with an infinite height[20] because the data at this position are less subjected to the end effects in inlets. These pressure rises and locations in the inlet were confirmed by those of two-dimensional inviscid shock-wave analysis.[20] The Pw increases from 0.36 to 1.2 up to the entrance of the isolator as a result of the impingement of the strut shock wave on the sidewall. The Pw decreases to 0.1 toward the exit of the engine. Downstream of the isolator, the Pw distribution indicates that the engine internal flow

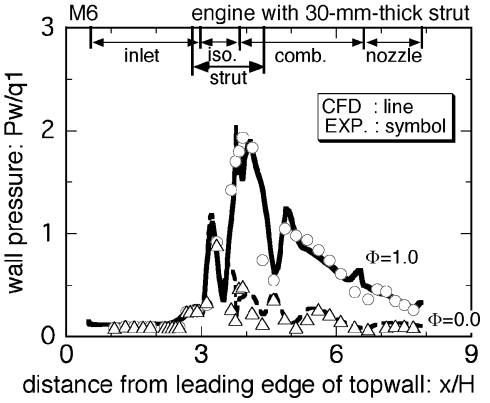

Fig. 3 Comparison of the numerical and experimental wall pressure distributions on sidewall: $y/H = 0.5$.

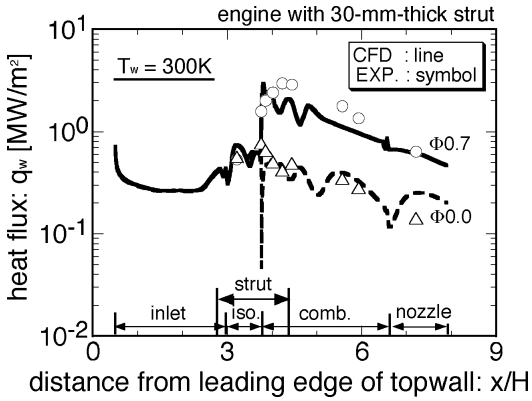

Fig. 4 Comparison of the numerical and experimental heat-flux distributions on sidewall: $y/H = 0.5$.

is supersonic. It can be seen that there is good agreement between the numerical and experimental results for this case.

For the combustion case shown by the solid line, the Pw up to the midpoint of the isolator is the same as that of the fuel-off. In the rear half of the isolator, there is a large pressure rise caused by the combustion. The combustion region is anchored in the near half of the isolator. Further downstream, the Pw varies because of the expansion and shock waves generated at the base region of the strut. These Pw implies that the combustion flow remains supersonic. Thus, the wall pressure distributions are helpful in understanding the appearance of the flow patterns inside the engine. The numerical result shows good agreement with the experimental data shown by the circular symbols.

2. Heat-Flux Distribution

The duplication of Pw by CFD is relatively easy. Accuracy of the CFD should be investigated by transport properties such as wall heating rate[21] qw or wall share stress τw. Comparisons of the qw are illustrated in Fig. 4. Computations are shown by lines and experimental heat-flux data by symbols. Experimental data have uncertainty of ±15% mentioned earlier. For the case of fuel-off shown by the broken line, the qw obtained by the computation is 0.8 MW/m^2 at the leading edge of the sidewall and rapidly decreases to 0.3 MW/m^2 up to $x/H = 1.0$. This high heating rate at the leading edge is attributed to the thinner boundary layer. The heat flux remains constant through the inlet and increases to 1.5 MW/m^2 in the isolator. The heat flux decreases to 0.2 MW/m^2 at the exit of the engine. The numerical results agree with the experimental results for this case.

For the combustion case shown by the solid line, the qw up to the isolator is the same as that of the fuel-off case. It increases up to 3 MW/m^2 at the entrance of the combustor and then decreases toward the exit of the engine. Downstream of the combustor, the qw of the combustion case is three- to four-fold of that in the fuel-off case because of high pressure and temperature produced by combustion. The heat-flux distribution for the case of fuel-air reacting shows good agreement with the experimental results shown by the circular symbols, too. Thus, comparison of the transport property qw as well as the Pw, verifies the present CFD code for both the fuel-off and the combustion cases.

B. Inlet Performance

1. Air Capture Ratio

The thrust of the engine is proportional to the amount of the air to be supplied into the combustor (captured air). If the captured air computed by the nonreactive CFD could not reproduce the experimental data, it is impossible to simulate the engine combustion tests. Figure 5 illustrates the computed dividing stream surface in the inlet with a 30-mm-thick strut. The upper wall is the cowl, and the lower wall is the topwall.

The dividing surface of the air spillage caused by the swept-shock system is traced backwards from the cowl lip to the front face of the inlet face in Fig. 5. The incoming flow under this surface is captured by the inlet. The height of the dividing surface at the inlet face is

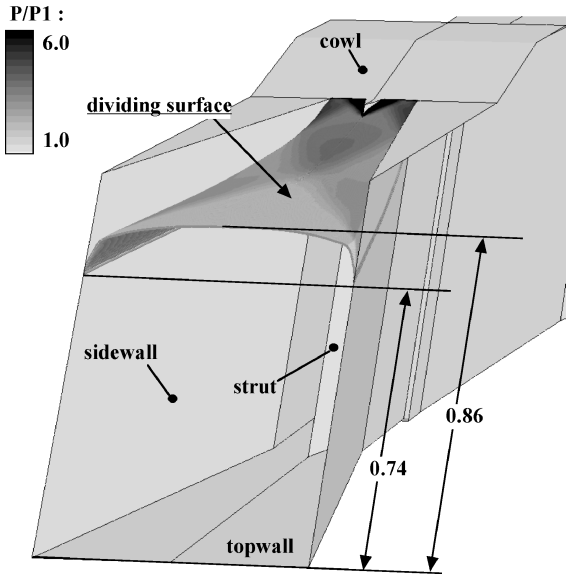

Fig. 5 Dividing surface and static pressure on the surface for evaluating the additive drag in the inlet with a 30-mm-thick strut.

termed captured height Hc in this paper. Most of the Hc start from the inlet face at a height of $y/H = 0.86$. The Hc decreases greatly from 0.86 to 0.74 as it approaches the wall. This is because the airflow near the wall greatly spills through the boundary layer.[22] From these capture heights, the air capture ratio η_c is found to be 0.83 by our viscous computation.

The η_c data of the same inlet have not been obtained under M6 condition in the experiment. Therefore, instead of the present inlet with 30-mm-thick strut, we used the η_c data measured in other conditions to verify the computed η_c. For example, in the inlet without a strut under M4 condition, the experimental η_c was 0.68 ± 0.02 (Ref. 23), and our computation was 0.70. In addition, the measured η_c in the inlet without a strut under M6 and M8 conditions were 0.88 ± 0.02 and 0.91 ± 0.02 (Ref. 24), and our computational η_c were 0.85 and 0.90 (Ref. 22), respectively. These computed η_c are in good agreement with the measured data, and we conclude that our computed η_c for the present inlet configuration is sufficiently accurate, too.

2. Additive Drag

The spillage produces additive drag in inlets D_{add}. The additive drag is calculated by momentum balance analysis for the control volume of the spilled stream tube. The control volume starts at the inlet face above the Hc and ends on the bottom of the inlet opening in front of the cowl in Fig. 5. The entrance momentum was 1830 N, and the exit momentum was found to be 1590 N. Therefore, the additive drag in the inlet resulted in a drag of $D_{\text{add}} = 240$ N. This additive drag is 21% of the inlet drag (Ref. 25) and is 28% of the engine internal drag ($D_{\text{int}} = 860$ N), which includes the positive force in the nozzle section.

The additive drag consists of two parts. One is the pressure drag working on the dividing surface. The other is the shear stress and pressure force on the sidewalls exposed to the spillage. In the momentum balance estimation, both the pressure drag on the dividing surface and the forces on the sidewalls cannot be separated from each other. To evaluate the pressure drag on the dividing surface, the static pressure P on the surface normalized by the upstream P_1 is shown in Fig. 5. The pressure ratio on the surface increases to more than six-fold of P_1 near the cowl lip caused by the shock waves. The shock waves generated at the leading edge of the sidewall cross each other at the centerplane and impinge on the opposite sidewall. The impinged shock waves are reflected back and cross the strut shock, resulting in a pressure ratio over 6.0. By integrating the pressure over the dividing surface in the streamwise, the pressure drag on the surface is found to be about 60 N, corresponding to 25% of the additive drag.

C. Thrust Increment with Combustion

Although the local τw is difficult to be directly measured, the engine drag/thrust can be measured in the engine tests. The drag and thrust are obtained from the integration of Pw and τw in the x direction. The accuracy of the τw is investigated by the comparison of engine drag/thrust in Fig. 6. Resultant engine internal drags D_{int} are summarized by the bar graphs in Fig. 6. The numerical D_{int} is 860 N. The friction drag (shaded area) dominates and occupies 80% of D_{int}. The numerical D_{int} coincides with experimental data measured in the subscale wind tunnel.[20] Especially, the friction drag agrees well. This good agreement indicates that our numerical prediction of τw is accurate.

Figure 6 illustrates the relationship between the fuel equivalence ratio Φ and the thrust increment ΔF. When the ΔF overcomes the D_{int}, the engine can push forward a space plane. Our engine obtains the net thrust over the $\Phi = 0.3 \sim 0.4$, as shown in Fig. 6. The solid line and open symbols denote the CFD results, and the broken lines and solid symbols show the experimental results. The symbols present both the results with the boundary-layer bleeding (circular symbols) and that without bleeding (triangle symbols).

In the experiment, two combustion modes were observed as shown by the broken lines. The lower line is termed a weak combustion mode (flame anchored downstream of the combustor), and the upper line is an intensive mode (flame attached to the entrance of combustor). In the engine tests, between the Φ of 0.3 and 0.7, the combustion mode switches from the weak mode to the intensive one and results in sudden increase of ΔF. In the experiments, the engine without boundary-layer bleeding falls into unstart at $\Phi = 0.48$ as shown by the solid triangle, just after the combustion mode switches from the weak mode to the intensive mode and a maximum ΔF of 1620 N is attained. When the boundary layer is bled 30 g/s, which corresponds to 0.6% of the captured air, the engine can start even in the intensive mode at this equivalence ratio. The start limit extends from $\Phi = 0.48$ to 1.0, and the maximum ΔF of 2460 N is achieved in the engine test.

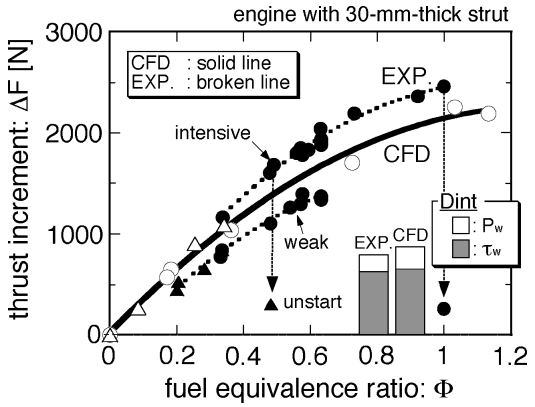

Fig. 6 Comparison of the numerical thrust increment with the experimental data, experimental uncertainty: ±100 N.

In contrast to the experimental results, there is no hysteresis of the ΔF in the computational results shown by the solid line. The ΔF increases continuously with increasing Φ. In the computations, the engine without bleeding falls into unstart at $\Phi = 0.5$ as is also the case for the experimental result. When the bleeding condition is applied, the engine starting limit extending from $\Phi = 0.5$ to 1.0 delivers a maximum ΔF of 2250 N in the CFD. Although the computed thrust shown by the solid line fails to duplicate the thrust jump between the two combustion modes, it can simulate the thrust dependence on Φ, and the values of ΔF at $\Phi = 1$ are in good agreement.

The computed ΔF is located between the weak and the intensive modes of the experiments. This is a limitation of CFD. Scramjet engines suffer a large drag in the inlet and produce a large thrust in the nozzle. A resultant (relatively small) increment is the net thrust. Therefore, the ΔF is greatly affected by slight errors in Pw. For example, a variation of ±2% in the computed Pw downstream of the combustor shown in Fig. 3 causes a large change of ±150 N in the thrust in Fig. 6. The change of combustion modes is probably governed by interaction between combustion and flow separations, which is affected by a turbulence model. Therefore, I believe that the accurate reproduction of the thrust jump is beyond the ability of the present CFD. We concluded that our computed thrusts agree with the experimental data except the thrust jump and confine us into gentle phenomenon in the engine. These comprehensive validation studies show that our CFD code is sufficiently accurate, and the physics in a real scramjet engine can be analyzed by our CFD.

IV. Simulations of Engine Combustion Test

A. Separation of Ingested Boundary Layer

Our engine is made of copper and is not cooled during the combustion tests. The wall temperature Tw increases from 300 to 600 K during the experiments.[8] The estimation of the Tw effects on the separation of the ingested boundary layer is important to understand the engine unstart mechanism. Figure 7 shows the limiting streamline patterns on the topwall obtained by the computation with two Tw conditions. Frame a is for an isothermal wall of 300 K ($Tw/T_1 \sim 1$), and frame b is for an adiabatic wall ($Tw/T_1 \sim 5$), which is the maximum possible Tw in our experiments. In these

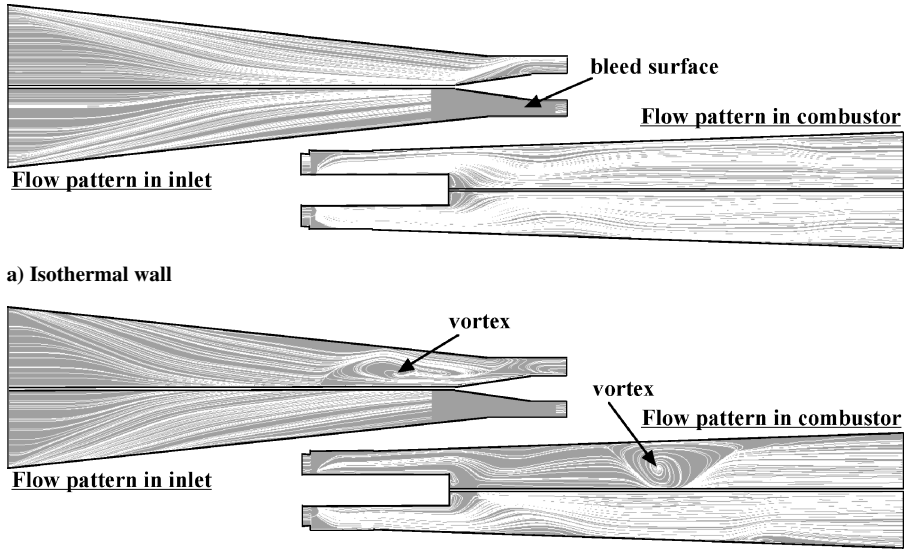

Fig. 7 Oil-flow patterns on the topwall with various wall temperature conditions with and without boundary-layer bleeding: upper half, without bleeding; lower half, with bleeding.

frames, the figures in the upper half are results without boundary-layer bleeding, and the lower ones are results with the bleeding.

In frame a, investigation of the inlet flow pattern for the isothermal condition shows that the surface patterns near the sidewall are identical to that of a single-fin interaction.[26] Here the well-known surface features include the upstream influence line, the primary separation line, and the primary attachment line. The result for the isothermal condition shows a weak interaction flow pattern between the crossing shock wave and the turbulent boundary layer.[27] In this flow, the primary separation lines of the two single fins turn parallel near the centerline. There is no centerline separation in this isothermal condition.

In frame b, the results for the adiabatic wall also show a weak interaction pattern.[27] However, the streamlines move upstream, and the inclination of both the separation line and the attachment line increase relative to the isothermal result. Moreover, a "bubble"-type separation can be seen upstream of the strut. Investigation of the flow pattern in the combustor shows that it is similar to that in the inlet. The inclination of streamlines on the adiabatic wall is greater than that of the isothermal wall, and there is a separation bubble generated by the impingement of the cowl shock in the middle of the combustor. This is because a high temperature near the adiabatic wall make the sonic velocity higher than that near the isothermal wall and extends the subsonic region in the boundary layer. Thus, the raise of the wall temperature caused a boundary-layer separation, which is highly undesirable in the operation of a high-speed inlet.

Once the fuel was injected, the adiabatic wall induced autoignition near the fuel injector at the cowl side, and the reaction zone expanded downstream of the engine by the convection of airflow. The heat was intensively released in the bubble-type separation caused by the impingement of the cowl shock as shown in Fig. 7b. This intensive heat release made the bubble larger and promoted its expansion toward the inlet. As the result, the numerical engine with adiabatic wall fell easily into the engine unstart even at very low Φ of 0.2.

The ignition in the M6 condition was sensitive to the wall temperature. Because the isothermal wall of 300 K did not extend combustion throughout the engine, the walls was impulsively heated to 1000 K during the first 0.5 ms. Once ignition was achieved, the wall temperature was assigned to be 300 K and fixed. The isothermal wall can keep the inlet supersonic (engine start condition) up to $\Phi = 0.5$ without the bleeding because there was no bubble-type separation on the topwall as shown in Fig. 7a.

To prevent the flow separations on the topwall, the ingested boundary layer was bled at a rate of 40 g/s, which was 0.65% of the captured air from the topwall. The bleeding flow rate was so low that there was no change in the nonreactive flowfield, except disappearance of the bubble separations upstream of the strut and at the impingement location of the cowl shock for the case of adiabatic wall. The suppression of the separation in the inlet reduced the pressure drag of strut, and the engine internal drag decreased by 100 N for this case, even though the compressed air in the inlet was discharged through the bleed surface. This bleeding can be able to extend the operating range and doubled the thrust in our computations for both the case of adiabatic wall and the isothermal wall of 300 K as discussed next.

B. Suppression of Engine Unstart with Boundary-Layer Bleeding

Figure 8 shows the numerically predicted Mach-number contours on $z/H = 0.3$ plane in the engine with the isothermal condition ($Tw = 300$ K) to investigate the state of the engine start and unstart conditions in detail. Frame a shows the result for the case of fuel-off without bleeding, and frame b is that of fuel-air reacting at $\Phi = 0.5$ without bleeding. Frames c and d show results for the fuel-off and combustion of $\Phi = 1.0$ cases with bleeding.

Frame a shows the shock and expansion waves and the boundary-layer development on the topwall. For example, the cowl shock impinges on the topwall at the middle of the combustor and is reflected back to the cowl. The boundary layer is found to be greatly thickened in the isolator and downstream of the impingement location of the cowl shock. The lower Mach-number (M2) regions can be seen on the topwall. From this flow pattern, it appears that the airflow remains supersonic throughout the engine (starting condition).

To quantitatively investigate the suppression mechanisms of engine unstart with boundary-layer bleeding, the boundary layer was measured numerically. Although the flow in the engine was complicated and it was difficult to define the edge of boundary layer, we defined it as the location where the turbulent eddy viscosity became minimum along lines normal to the walls. Accordingly, the thickness of velocity boundary layer was found to increase from 50 mm at the entrance of the inlet to 110 mm at the entrance of the combustor on the topwall. The momentum thickness of the topwall boundary layer developed from 2.92 mm at the entrance of the inlet to 4.9 mm at the entrance of the combustor.

Frame b for the combustion case shows typical engine unstart. A strong shock wave runs from the leading edge of the topwall to the cowl side, and the inlet flow is found to be completely different from that in frame a. This strong shock wave is caused by the boundary-layer separation as a result of combustion. About 80% of

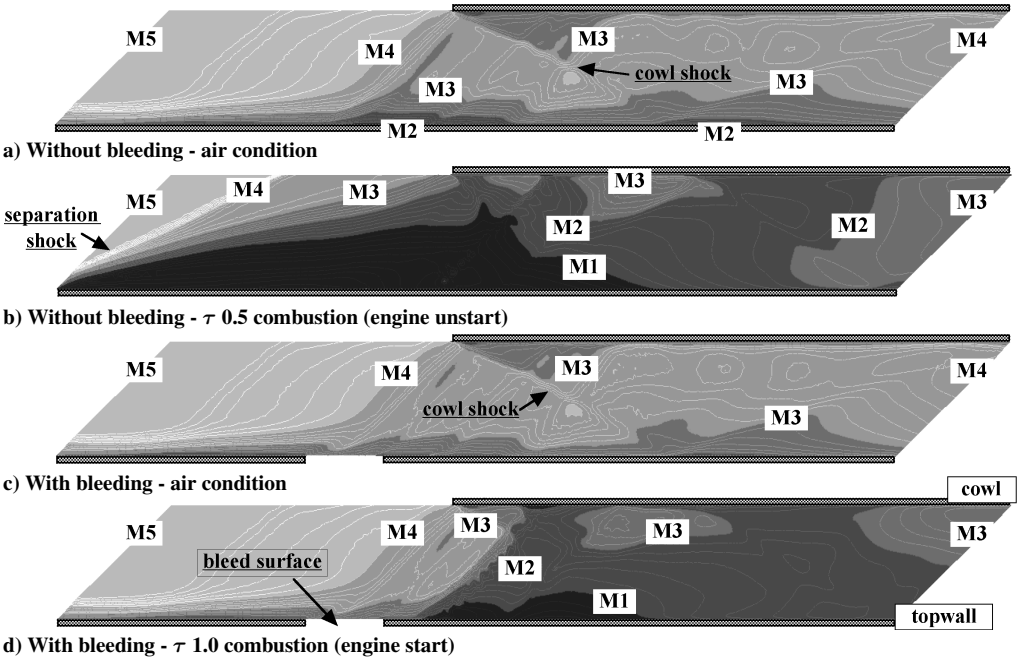

Fig. 8 Numerical prediction of Mach number with/without boundary-layer bleeding.

the incoming flow spills from the inlet, and a large subsonic region is generated behind this shock wave. This subsonic flow is accelerated downstream of the isolator and exhausted from the engine exit with supersonic speed. Thus, the engine without bleeding is stalled by separation of the ingested boundary layer on the top-wall.

The ingested boundary layer is bled at a rate of 0.65% of the captured air from the topwall in frames c and d. Frame c for the fuel-off case shows that the lower Mach number (M2) region on the topwall downstream of the bleed surface becomes thinner than that without bleeding shown in frame a. Even though the boundary layer was bled, the speed of the outer boundary layer and the thickness of velocity boundary layer hardly changed because of the lower bleeding flow rate. As the result, the thickness of momentum boundary layer decreased from 4.9 to 3.5 mm with bleeding at the entrance of the combustor on the topwall. The momentum thickness in the isolator on the topwall decreases 30% resulting from 0.65% of bleeding.

Once fuel is injected, there is a significant decrease of Mach number in the combustor and the nozzle as shown in frame d. A low-Mach-number region is formed just behind the injector section, and one-third of the engine height near the topwall is occupied by the subsonic region in the isolator. This subsonic region in the isolator was caused by ascent of the combustion region with the boundary-layer separation. However, the combustion region could not ascend upstream of the bleed surface, and there is no change in the inlet. Thus, the engine with bleeding does not fall into unstart even at $\Phi = 1.0$, and the combustion flowfield consisted of the large supersonic region, and the small subsonic region is formed as a result of the intense combustion.

C. Flame Structure in Scramjet Combustor

Combustion flowfields obtained by our numerical simulations can be used to understand the physics governing the engine combustion performance. Figure 9 shows the mass fraction of the OH radicals at $\Phi = 1.0$. This figure reveals the flame structure in the engine, which controls the combustion performance. The left of Fig. 9 shows the three-dimensional view of the OH radical distributions in the engine. The right portion of Fig. 9 shows the cross-sectional contours inside the engine. Frame a is the section near the fuel injectors. Frames c and f are those just behind the strut and at the exit of the engine, respectively.

Frame a shows the small discrete circular flames shown by the OH radical around individual fuel jets. There are two intense combustion zones in frame a. One is the dark region around the four fuel jets near the cowl. Combustion in this region is intensified by the high temperature and pressure behind the cowl shock. The other is the dark region near the topwall. In this region, two jets closest to the topwall show higher penetration into the main flow, and they reach the wall of the strut. This is because they are embedded in the subsonic region caused by the combustion shown in Fig. 8d.

Further downstream, frame b shows that the circular flame structures disappear to form a couple of envelope flames from the cowl to the topwall. This is because the oxygen between the fuel jets is completely consumed. These envelope flames show two intense combustion zones (cowl side and topwall side) similar to those of frame a. These flames are found to be diffusion flames[24] because unburned H_2 did not coexist with O_2 at either side of the OH peaks in Fig. 9.

The flame configuration changes downstream of the strut as shown by frames c–f. The OH radicals are distributed at the core flow as well as near the sidewall in these pictures. This is caused by the secondary flow in the boundary layer induced by the large pressure difference across the cowl shock and combustion region. The H_2 of cowl side is carried to the topwall by the secondary flow and merged with the H_2 on the topwall. As the result, a huge mass of unburned H_2 is generated on the topwall. The unburned H_2 flows into the recirculation region behind the strut. This fuel jet is pushed up toward the cowl by the large pressure difference as a result of the intensive combustion at the topwall side and make a couple of vortices in the wake of the strut. Around the rim of these vortices, the fuel burns, and the OH radicals are generated as shown by the images in frames c–f. Thus, in our scramjet engine, small-separated flame structures are disappeared by the flow distortion caused by the cowl shock.

These flame structures controlled the combustion efficiency in the engine. Finally, the bulk combustion efficiency was investigated in our numerical engine. The combustion efficiency was defined as the ratio between the H_2 consumption rate and the H_2 supply rate. The computational combustion efficiency increased from zero at $x/H = 3.3$ to 0.45 at $x/H = 3.9$ and became saturated at 0.55 at the exit of the engine ($x/H = 7.4$) (Ref. 25). The rapid increase of combustion efficiency was attributed to small-separated circular flames formed around individual jets. Thus, small-separated flames around individual jets produced 80% of the combustion efficiency and mainly delivered a thrust as reported in Ref. 25. On the other hand, Diskin and Northam[28] and Masuya et al.[29] experimentally evaluated combustion efficiency in scramjet combustor models in which there was no distortion. In their experiments, the combustion efficiencies were very high (about 90%). Therefore, the large-merged flame downstream of the combustor in our engine was found to restrict combustion efficiency. The alleviation of the flow distortion at the entrance of the combustor produced by the cowl shock is urgent for the improvement of the engine performance.

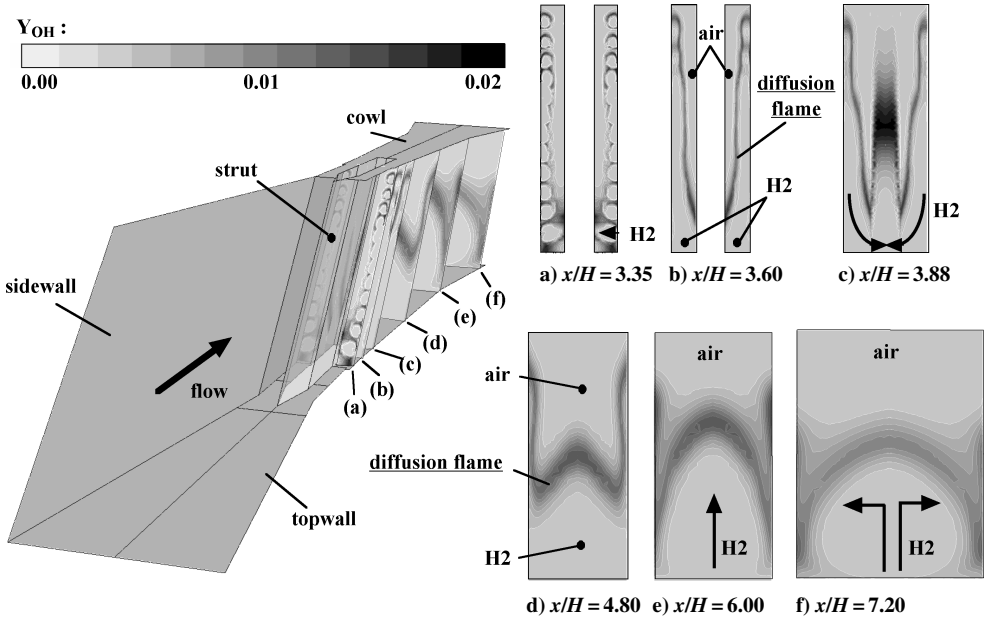

Fig. 9 Numerically predicted crossflow OH mass fraction: a) fuel injection, c) strut base, f) engine exit.

V. Conclusions

Numerical simulations of a scramjet engine with and without boundary-layer bleeding were performed under Mach 6 flight conditions by a three-dimensional Reynolds-averaged Navier–Stokes flow code with finite-rate chemistry. The following conclusions were drawn:

1) Numerical results of the wall pressure distributions and transport properties such as heat flux in the fuel-off case and the combustion case showed good agreement with the experimental data. In addition to these calibrations, our computations reproduced the experimental thrust data.

2) Inlet performance was estimated from investigation of the dividing stream surface and compared with results of the aerodynamic tests. The air capture ratio of the inlet was 0.83, and the additive drag caused by the spillage was found to account for 28% of the internal drag. The computed air capture ratio also agreed well with the experimental data.

3) The effect of wall temperature on boundary-layer separation in the engine was investigated. Switching the wall boundary condition from an isothermal wall of 300 K to an adiabatic wall ($\sim$1500 K), the boundary layer on the topwall separated around the leading edge of the strut and the location of impingement on the cowl shock. These separations easily caused engine unstart when combustion occurred.

4) The engine with the isothermal wall fell into engine unstart at $\Phi = 0.5$. The boundary-layer bleeding prevented the flow separation and extended the start limit. Bleeding of 0.6% in the captured air extended the start limit from $\Phi = 0.5$ to 1.0. The computations well reproduced the combustion tests with bleeding.

5) Computation at $\Phi = 1.0$ showed that circular diffusion flames were formed around individual jets near the fuel injectors. In the downstream region, these circular structures disappeared to form a large-scale envelope diffusion flame. These circular flames at the narrow region near the injectors governed the combustion performance.

Acknowledgment

This work was partly supported by the Japan Society for the Promotion of Science (JSPS) through Grant 15007299. The first author wishes to thank the JSPS for its financial support. We are especially indebted to Masatoshi Kodera and Yasushi Ito for their help with hybrid unstructured grid generations.

References

[1]Mitani, T., Sakuranake, N., Tomioka, S., and Kobayashi, K., "Boundary Layer Bleed and the Effects in Scramjet Engines in Mach 4 and 6," *Journal of Propulsion and Power* (to be published).

[2]Kodera, M., Tomioka, S., Kanda, K., Mitani, T., and Kobayashi, K., "Mach 6 Test of a Scramjet Engine with Boundary-Layer Bleeding and Two-Staged Fuel Injection," AIAA Paper 2003-7049, Dec. 2003.

[3]Hosangadi, A., Ungewitter, R., Cavallo, P. A., and Dash, S. M., "Unstructured Navier–Stokes Code Simulation of Scramjet Combustor Flowfields," AIAA Paper 99-4899, Nov. 1999.

[4]Goyne, C. P., MacDaniel, J. C., Quagliaroli, T. M., Krauss, R. H., MacDaniel, J. C., and Day, S. W., "Dual-Mode Combustion of Hydrogen in a Mach 5, Continuous-Flow Facility," *Journal of Propulsion and Power*, Vol. 17, No. 6, 2001, pp. 1313–1318.

[5]Goyne, C. P., Rodriguez, C. G., Krauss, R. H., MacDaniel, J. C., and MaClinton, C. R., "Experimental and Numerical Study of a Dual-Mode Scramjet Combustor," AIAA Paper 2002-5216, Sept. 2002.

[6]Kodera, M., Sunami, T., and Nakahashi, K., "Numerical Analysis of Scramjet Combusting Flows by Unstructured Hybrid Grid Method," AIAA Paper 2000-0886, Jan. 2000.

[7]Kobayashi, K., Tomioka, S., and Mitani, T., "Supersonic Flow Ignition by Plasma Torch and H2/O2 Torch," *Journal of Propulsion and Power*, Vol. 20, No. 2, 2004, pp. 294–301.

[8]Hiraiwa, T., Kobayashi, K., Wakamatsu, Y., and Mitani, T., "Heat Flux on Scramjet Engine at Mach 4 Flight Condition and Heat Flux Meter Evaluation," *Proceedings of the 4th Symposium on Propulsion System for Reusable Launch Vehicles*, Northern Section of the Japan Society for Aeronautical and Space Sciences, May 2003, pp. 197–202 (in Japanese).

[9]Mitani, T., Tomioka, S., Kanda, T., Chinzei, N., and Kouchi, T., "Scramjet Performance Achieved in Engine Tests from M4 to M8 Flight Conditions," AIAA Paper 2003-7009, Dec. 2003.

[10]Kouchi, T., Mitani, T., Hiraiwa, T., Tomioka, S., and Masuya, G., "Evaluation of Thrust Performance in Scramjet Engines with Measured Internal Drag," *Journal of the Japan Society for Aeronautical and Space Science*, Vol. 51, No. 595, 2003, pp. 403–411 (in Japanese).

[11]Wada, Y., and Liou, M. S., "A Flux Splitting Scheme with High-Resolustion and Robustness for Discontinuities," AIAA Paper 94-0083, Jan. 1994.

[12]Venkatakrishnan, V., "On the Accuracy of Limiters and Convergence to Steady State Solutions," AIAA Paper 93-0880, Jan. 1993.

[13]Sharov, D., and Nakahashi, T., "Reordering of 3-D Hybrid Unstructured Grids for Lower-Upper Symmetric Gauss-Seidel Computations," *AIAA Journal*, Vol. 36, No. 3, 1998, pp. 484–486.

[14]Chase, M. W., Jr., Davies, C. A., Downey, J. R., Jr., Frurip, D. J., McDonald, R. A., and Syverud, A. N., "JANAF Thermochemical Tables, 3rd Edition," *Journal of Physical and Chemical Reference Data*, Vol. 14, No. 1, 1985, pp. 1211, 1248, 1253, 1260, 1274, 1280, 1551, 1639, 1667.

[15]Stahl, G., and Warnatz, J., "Numerical Investigation of Time Dependent Properties and Extinction of Structure of Methane and Propane Air Flamelets," *Combustion and Flame*, Vol. 85, June 1991, pp. 285–299.

[16]Goldberg, U. C., and Ramakrishnan, S. V., "A Pointwise Version of Baldwin-Barth Turbulence Model," *Computational Fluid Dynamics Journal*, Vol. 1, 1993, pp. 321–338.

[17]Kodera, M., Nakahashi, T., Hiraiwa, K., Kanda, T., and Mitani, T., "Scramjet Inlet Flow Computations by Hybrid Grid Method," AIAA Paper 98-0962, Jan. 1998.

[18]Miyajima, H., etc., RJTF Construction Group, "Ramjet Engine Test Facility," National Aerospace Lab., NAL TR-1347, Tokyo, Feb. 1998 (in Japanese).

[19]Ito, Y., and Nakahashi, K., "Improvements in the Reliability and Quality of Unstructured Hybrid Mesh Generation," *International Journal for Numerical Methods in Fluids*, Vol. 45, No. 1, May 2004, pp. 79–108.

[20]Tarukawa, Y., Mitani, T., Hiraiwa, T., and Masuya, G., "Three-Compnent Force Estimation for Scramjet Engines—1) Engine Drag from Mach 4 to Mach 8 Flight Conditions," *Journal of the Japan Society for Aeronautical and Space Science*, Vol. 51, No. 592, 2003, pp. 244–251 (in Japanese).

[21]Kouchi, T., Mitani, T., Hiraiwa, T., Kodera, T., and Masuya, G., "Heat Flux Prediction for Scramjet—Accuracy of Reynolds Analogy on Scramjet Internal Walls," *Proceedings of the 24th International Symposium on Space Technology and Science*, edited by J. Onoda, Oct. 2004, pp. 20–26.

[22]Kouchi, T., Mitani, T., Kodera, T., and Masuya, G., "Effects of Reynolds Number on Scramjet Inlet Performance," *Proceedings of the 23rd International Symposium on Space Technology and Science*, edited by N. Ishii, Vol. 2, Nov. 2002, pp. 2412–2417.

[23]Kitamura, E., Mitani, T., Sakuranaka, N., and Masuya, G., "Evaluating the Aerodynamic Performance of Scramjet Engines by Pressure Measurement," AIAA Paper 2003-7053, Dec. 2003.

[24]Tani, K., Kanda, T., and Tokunaga, T., "Starting Characteristics of Scramjet Inlets," *Proceedings of 11th ISABE*, edited by F. S. Billig, Vol. 1, 1993, pp. 1071–1080.

[25]Mitani, T., and Kouchi, T., "Flame Structures and Combustion Efficiency Computed for a Mach 6 Scramjet Engine," *Combustion and Flame* (to be published).

[26]Garrison, T. J., and Settles, G. S., "Interaction Strength and Model Geometry Effects on the Structure of Crossing-Shock Wave/Turbulent Boundary-Layer Interactions," AIAA Paper 93-0780, Jan. 1993.

[27]Settles, G. S., and Dolling, D. S., "Swept Shock/Boundary-Layer Interactions-Tutorial and Update," AIAA Paper 90-0375, Jan. 1990.

[28]Diskin, G. S., and Northam, G. B., "Effects of Scale on Supersonic Combustor Performance," AIAA Paper 87-2164, Jan. 1987.

[29]Masuya, G., Uemoto, T., Wakana, Y., Kudou, K., Murakami, A., and Komuro, T., "Performance Evaluation of Scramjet Combustors Using Kinetic Energy and Combustion Efficiencies," *Journal of Propulsion and Power*, Vol. 15, No. 3, 1999, pp. 401–407.